Applied Surface Science 685 (2025) 162094

Contents lists available at ScienceDirect

Applied Surface Science

journal homepage: www.elsevier.com/locate/apsusc

Full Length Article

Synthesis of yolk-shell structured microspheres consisting of heterogeneous nickel cobalt selenide@nickel cobalt selenite core–shell nanospheres and their application of anode materials for sodium-ion batteries

Yeong Beom Kim [a,b,‡], Seong-Yong Jeong [c,‡], Jung Sang Cho [d], Dong-Hee Lim [e,*], Yun Chan Kang [b,*], Gi Dae Park [a,f,*]

[a] Department of Advanced Materials Engineering, Chungbuk National University, Chungdae-ro 1, Seowon-gu, Cheongju 28644, Republic of Korea
[b] Department of Materials Science and Engineering, Korea University, Anam-Dong, Seongbuk-Gu, Seoul 136-713, Republic of Korea
[c] Department of Advanced Materials Engineering, Kongju National University, Cheonan, Chungnam 31080, Republic of Korea
[d] Department of Engineering Chemistry, Chungbuk National University, Chungdae-ro 1, Seowon-gu, Cheongju 28644, Republic of Korea
[e] Department of Environmental Engineering, Chungbuk National University, Chungdae-ro 1, Seowon-gu, Cheongju 28644, Republic of Korea
[f] Advanced Energy Research Institute, Chungbuk National University, Chungdae-ro 1, Seowon-gu, Cheongju 28644, Republic of Korea

ARTICLE INFO

Keywords:
Heterostructure
Hollow nanosphere
Nanoscale Kirkendall effect
Yolk-shell structure
Sodium-ion batteries

ABSTRACT

Recently, heterostructure interfaced construction by binary metal selenide or metal oxide/metal selenide configuration has been attracting attention as anodes for sodium-ion batteries (SIBs). Especially, modification strategies such as formation of core–shell structure consisting of heterointerface can be a solution to resolve the issue of metal selenide electrodes. In this paper, new multicomponent metal compounds with heterointerface structure are firstly designed and suggested as anode for SIBs. The yolk-shell microsphere consisting of heterogeneous NiCo selenide@NiCo selenite core–shell nanospheres was prepared by spray pyrolysis and facile selenization and subsequently partial oxidation processes. NiCo selenide nanocrystals, which constitute the yolk-shell structure, are partially transformed into the NiCo selenide@NiCo selenite phase during the oxidation process. Notably, this process induces the nanoscale Kirkendall effect, leading to the transformation of the metal selenide nanocrystals into a hollow nanosphere morphology. As a result, the material adopts a hollow nanosphere structure with a NiCo selenide@NiCo selenite core–shell configuration. To the best of our knowledge, metal selenide@metal selenite core–shell configuration with hollow nanosphere is proposed for the first time. Heterointerface as well as yolk-shell structure consisting of hollow nanospheres showed synergistic effect for efficient and excellent sodium ion storage.

1. Introduction

Recently, sodium-ion batteries (SIBs) have gained attention as an alternative to lithium-ion batteries (LIBs) because of the wide availability of sodium resources [1–4]. In the process of researching suitable anodes for SIBs, metal selenides are evaluated as a strong anode candidate based on their high theoretical capacities and the large slab space between their 2-D planes [5–8]. However, metal selenides are hindered by their inherently low electronic conductivity and structural degradation caused by significant volume changes during cycling [9,10]. Furthermore, the dissolution of selenium due to soluble polyselenide intermediates during the Na_2Se formation and decomposition process leads to capacity degradation, ultimately impeding their practical viability [11,12].

To correct above critical issues, modification strategies such as coating with carbonaceous material including nanostructure have been applied to resolve issues of metal selenides electrodes [13,14]. Polydopamine such as conductive polymer coating and its decomposed carbon coated metal selenides were diversely reported as anode materials for SIBs. Liu et al. synthesized heterostructure $SnSe_2$/ZnSe@polydopamine nanobox by co-precipitation method, selenization, and coating process in liquid phase [15]. The conductive and flexible polydopamine shell can serve as a protective buffer for the $SnSe_2$/ZnSe yolk, effectively mitigating pulverization and aggregation issues during

* Corresponding authors.
E-mail addresses: limkr@cbnu.ac.kr (D.-H. Lim), yckang@korea.ac.kr (Y.C. Kang), gdpark@chungbuk.ac.kr (G.D. Park).
‡ These authors contributed equally to this work.

https://doi.org/10.1016/j.apsusc.2024.162094
Received 17 September 2024; Received in revised form 28 November 2024; Accepted 12 December 2024
Available online 13 December 2024

cycling. Metal-organic frameworks derived metal selenides were mostly coated by nitrogen-doped carbon component by in-situ carbon encapsulating during heat-treatment, which was applied to anode materials for SIBs [16,17].

Recently, heterostructure interface construction by binary metal selenide or metal oxide/metal selenide configuration has been attracting attention due to the various advantages, which were derived from heterointerfaces [18,19]. Specifically, bimetallic compounds consisting of two transition metals demonstrate a synergistic effect, resulting in improved electrochemical performance compared to single metal compounds [20–23]. This improvement is primarily due to the broader range of electrochemical redox reactions and the synergistic interactions between different transition metal atoms [24,25]. Li *et al.* reported the fabrication of CoSe/$MoSe_2$-C nanosphere heterostructure *via* facile solvothermal process, and simultaneous selenization and carbonization strategies [26]. The heterostructure combines the advantages of both CoSe and $MoSe_2$ simultaneously, which is favorable for sodium ion storage as well as lowering the ion diffusion energy barrier and thus enabling rapid charge transfer. Zhao *et al.* developed MoO_2 nanoclusters anchored on two-dimensional (2D) $MoSe_2$-graphene interfaces, enhancing the reversible conversion of $MoSe_2$ for use as a long-lasting anode in sodium-ion batteries and sodium-ion capacitors [27].

In this paper, we designed and suggested new multicomponent metal compounds with heterointerface structure. The yolk-shell structured microsphere consisting of heterogeneous NiCo selenide@NiCo selenite core–shell nanospheres was prepared by spray pyrolysis and facile selenization and subsequently partial oxidation processes. The NiCo oxide yolk-shell microspheres were fabricated by single-step spray pyrolysis. By employing spray pyrolysis, the yolk-shell configuration was efficiently synthesized without the need for a template method, enabling rapid and eco-friendly preparation. During the subsequent selenization, these microspheres were transformed into NiCo selenide while preserving the yolk-shell configuration. NiCo selenide nanocrystals, which form a yolk-shell structure, undergo partial oxidation with the nanoscale Kirkendall effect. This process transforms each nanocrystal into a hollow nanosphere with a NiCo selenide@NiCo selenite core–shell structure, preserving the overall yolk-shell configuration. The void space arising from the yolk-shell and hollow nanosphere structures not only acts as a buffer space to alleviate the volumetric stress generated during cycling but also shortens the path for Na-ions, thereby enhancing the rate capability. To the best of our knowledge, metal selenide@metal selenite core–shell structure with hollow nanosphere is proposed for the first time. After sodiation and desodiation processes, binary NiCo selenide@NiCo selenite is converted into each single component selenide@-metal oxide/selenium oxide form as reported in the previous literatures. The diverse heterointerfaces facilitate rapid charge transfer kinetics, lower the sodium diffusion barrier, and effectively mitigate polyselenide dissolution through strong adsorption interactions between the metal selenide and metal oxide [27]. As expected, the unique integration of heterointerfaces and yolk-shell structures, featuring hollow nanospheres, exhibited a synergistic effect by providing exceptional structural stability and significantly enhancing sodium-ion transport.

2. Experimental

The NiCo oxide yolk-shell microspheres were prepared via spray pyrolysis. To prepare the spray solution, 0.1 M cobalt nitrate hexahydrate, 0.1 M nickel nitrate hexahydrate, and 0.7 M sucrose were dissolved in 1 L of distilled water. This mixture was then atomized with a 1.7-MHz ultrasonic spray generator that features six vibrators. The droplets, carried by air flowing at 10 L/min, were carried into a quartz reactor with 50 mm of diameter and 1200 mm of length, kept at 700 °C. The spray precursor, along with selenium powder, underwent post-treatment in a tube furnace at 300 °C under a 5% H_2/Ar atmosphere for 12 h, leading to the formation of NiCo selenide yolk-shell microspheres. To form the heterointerface, the NiCo selenide yolk-shell microspheres were further post-treated at various temperatures (400, 450, and 500 °C) in an air atmosphere. Extensive information regarding the characterization and electrochemical evaluation is provided in the Supporting Information.

3. Results and discussion

The formation mechanism of the yolk-shell structured microsphere consisting of heterogeneous NiCo selenide@NiCo selenite core–shell nanospheres was described in Scheme 1. Firstly, the yolk-shell structured NiCo oxide microspheres were fabricated by spray pyrolysis method. The droplet (Scheme 1a-1) containing nickel and cobalt nitrate and sucrose, which was formed from spray solution by spray generator, was transformed into NiCo oxide yolk-shell microspheres (Scheme 1a-2) via repeated combustion/contraction processes, as outlined in previous study [28]. The synthesized NiCo oxide yolk-shell microspheres underwent selenization using selenium powder through heat treatment in a reducing atmosphere. The yolk-shell configuration consisting of NiCo selenide nanocrystals was obtained as described in Scheme 1a-3. To construct the heterointerface, NiCo selenide yolk-shell microspheres (labeled as NCSe-YS) were changed into various composition complexes (NiCo selenide@NiCo selenite, NiCo selenite@NiCo oxide, and NiCo oxide configuration) through an oxidation process at 400, 450, and 500 °C, respectively, with the resulting samples denoted as NCSe@NCSeO-YS, NCSeO@NCO-YS, and NCO-YS, as illustrated in Scheme 1b-1-3. Among the oxidation processes at each temperature, the formation mechanism for hollow nanosphere with heterointerface *via* a well-known Kirkendall diffusion effect at the nanoscale, is depicted in Scheme 1c. In the thermal oxidation, the diffusion rates of Ni, Co, and Se components exceeded that of O_2 gas. The outward movement of these components toward the surface of the NiCo selenide@NiCo selenite intermediate resulted in the formation of a hollow cavity at 400 °C [29]. Through a continuous oxidation process, NiCo selenide is converted to NiCo selenite, and the outermost shell forms a NiCo oxide layer at 450 °C. Finally, it is completely converted to a pure NiCo oxide phase at a temperature of 500 °C, and the hollow nanosphere structure is densely converted by sintering.

The morphological properties of NiCo oxide yolk-shell microspheres, which were prepared by single-step spray pyrolysis method, were displayed in Fig. S1. The low-magnified SEM image (Fig. S1a) revealed that there was a slight deviation in the size distribution of all spherical microsphere. It was attributed to size variations of droplets, which were formed by spray generator. The one droplet was decomposed and formed to one microsphere. The high magnified SEM image (Fig. S1b) revealed the development of yolk-shell configuration in the microspheres. The formed sprayed precursor yolk-shell powder represented the NiO-$NiCo_2O_4$ composite phase as indicated by the XRD results in Fig. S1c. It might be attributed to the production of the precursor using the spray solution with Ni and Co 1:1 M ratio. The NiCo oxide yolk-shell microspheres were successfully converted into the NiCo selenide yolk-shell microsphere (NCSe-YS), and their morphologies represented that yolk-shell structure was kept well as shown in Fig. S2a and S2b. The crystal structure of NCSe-YS exhibited mixed nickel and cobalt selenide phases as revealed by XRD data in Fig. S2c.

The NCSe-YS sample was oxidized at 400, 450, and 500 °C, respectively, and their morphological and crystal structures were concretely investigated. The morphological characteristic of NCSe@NCSeO-YS, which was prepared at oxidation of 400 °C, was exhibited in Fig. 1. The SEM images in Fig. 1a and b revealed that yolk-shell structure was well maintained after oxidation from NCSe-YS. The TEM images in Fig. 1c and d clearly show the formation of an inner yolk@void@shell structure, as well as a distinct hollow nanosphere configuration after the oxidation process. The formation of the hollow nanospheres is attributed to the creation of NiCo selenide@NiCo selenite through nanoscale Kirkendall diffusion. Detailed TEM images presented in Fig. 1e and f illustrate the morphology of the small-sized hollow nanospheres. By

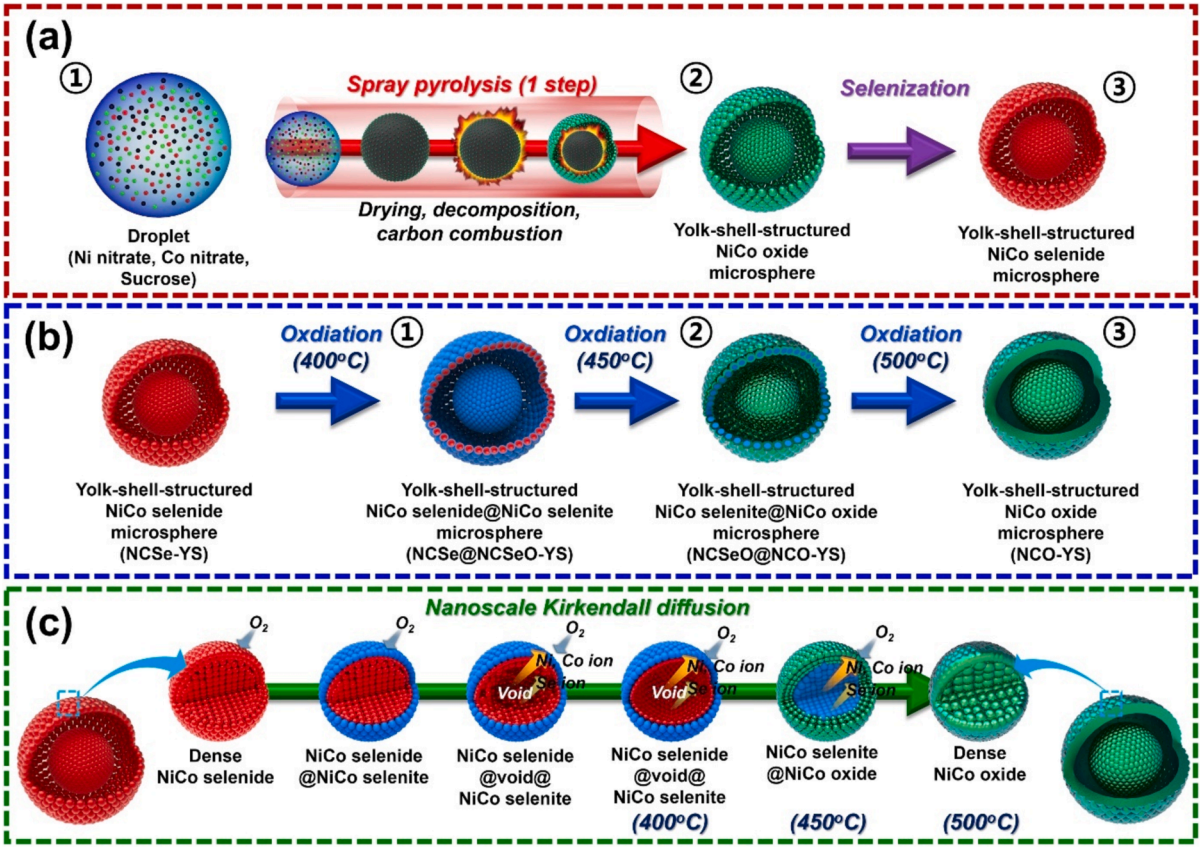

Scheme 1. Schematic illustration of (a) formation mechanisms for yolk-shell structured NiCo selenide microsphere via spray pyrolysis and subsequent selenization process, (b) oxidation process at various temperatures to synthesize yolk-shell microspheres with different compositions, and (c) formation of hollow-structured NiCo selenide@NiCo selenite nanocrystals via nanoscale Kirkendall diffusion, followed by a gradual sintering process that becomes more pronounced at higher temperatures, resulting in densely structured NiCo selenite@NiCo oxide and NiCo oxide nanocrystals.

different diffusion rate between nickel, cobalt, selenium, and oxygen, dense structured NiCo selenide nanocrystals were transformed into NiCo selenide@NiCo selenite core–shell structured hollow nanospheres. Fig. 1g presents a high-resolution (HR) TEM image showing clear lattice fringes with spacings of 0.29 and 0.24 nm. These measurements correspond to the (423) and (211) crystal planes of the NiCo selenide and NiCo selenite phases, respectively. Selected area electron diffraction (SAED) patterns in Fig. 1h confirmed the presence of NiCo selenide and NiCo selenite phases in of yolk-shell microsphere consisting of NiCo selenide@NiCo selenite nanocrystals. Fig. 1i displays elemental mapping images that vividly illustrate the development of a yolk-shell structured microsphere with metal selenide and metal selenite components.

The morphologies of yolk-shell microspheres, which were synthesized at oxidation of 450 and 500 °C (NCSeO@NCO-YS and NCO-YS, respectively), were shown in Fig. 2. Even though oxidation at higher temperature than 400 °C, overall microsphere retained yolk-shell structure as displayed in Fig. 2(a)-2(d). High magnified SEM images (Fig. 2b and d) verified that the size of nanocrystals consisting of yolk-shell microspheres was gradually increased as oxidation occurs at a higher temperature. On the other hand, the crystal structures of three yolk-shell microspheres, which were prepared at oxidation 400, 450, and 500 °C, respectively, were confirmed to vary depending on temperature, as shown in Fig. 2e, while the yolk-shell configuration remained consistent during the oxidation process. From the XRD analysis (Fig. S2c), the mixed nickel and cobalt selenide phases of NCSe-YS were identified. Following the oxidation process at 400 °C for 9 h, the surface of the (Ni,Co)Se_2 nanocrystals was converted to the (Ni,Co)SeO_3 phase, as indicated by the XRD data in Fig. 2e. For a sufficiently long oxidation time, as confirmed in the TEM results of Fig. 1e and f, voids were formed inside the nanocrystals due to the nanoscale Kirkendall diffusion effect, forming hollow nanospheres. When the temperature was slightly raised and oxidized at 450 °C, all (Ni,Co)Se_2 nanocrystals were oxidized, and a mixed phase of (Ni,Co)SeO_3, NiO, and $NiCo_2O_4$ was formed. After the high oxidation temperature at 500 °C, (Ni,Co)SeO_3 phase was vanished and finally, mixed NiO and $NiCo_2O_4$ phases were observed as shown in Fig. 2e. To further validate the structural and compositional changes resulting from the oxidation temperature, TEM analysis was conducted on the NCSeO@NCO-YS and NCO-YS samples. As shown in Fig. S3a-d, the TEM images of these samples reveal yolk-shell morphologies consistent with their SEM results. However, compared to the TEM image of the NCSe@NCSeO-YS sample (Fig. 1), these samples exhibit larger crystal sizes due to high-temperature oxidation. Notably, the nanocrystals (or nanospheres) in these samples were observed to exhibit a dense structure rather than a hollow morphology, likely due to sintering during the oxidation process. In fact, the nanocrystals within each sample were observed to exist in a range of sizes. To provide a detailed analysis, we measured the crystal (nanosphere) sizes present in the samples and represented their distribution curves, as shown in Fig. S4. Consequently, it was found that, compared to NCSe@NCSeO-YS, the NCSeO@NCO-YS sample exhibited a slightly larger crystal size distribution, while the NCO-YS sample showed a significantly larger crystal size distribution. In addition to their dense structure, the larger crystal sizes increase the Na-ion diffusion path inefficiently and reduce the number of active sites for Na-ion interaction, ultimately leading to decreased electrochemical reactivity. Moreover, the HR-TEM images and SAED patterns (Fig. S3e-h) confirm that the nanocrystals present in each sample are composed of NiCo

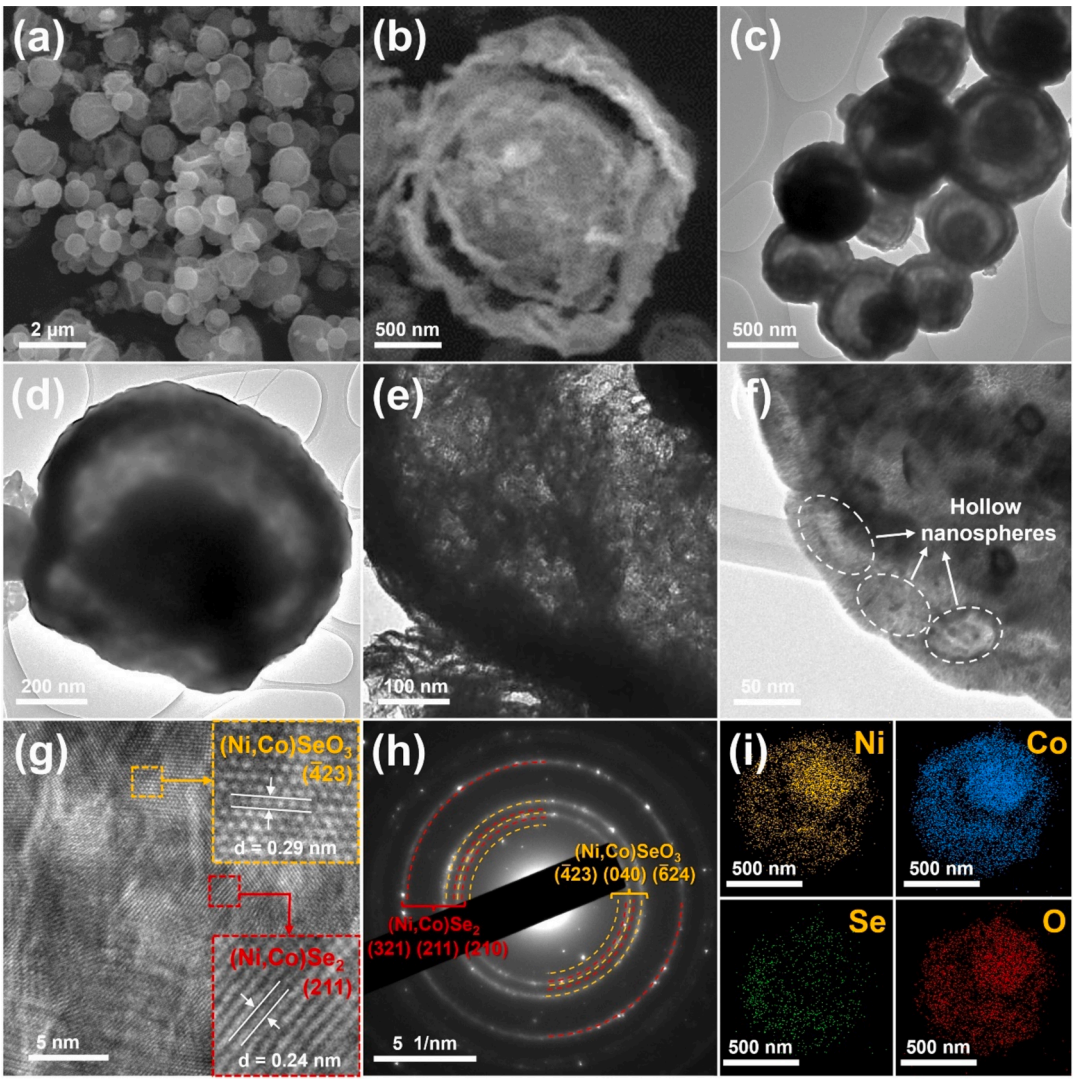

Fig. 1. Morphological characteristics of NCSe@NCSeO-YS: (a,b) SEM images, (c-f) TEM images, (g) HR-TEM image, (h) SAED pattern, and (i) elemental mapping images.

selenite@NiCo oxide (NCSeO@NCO-YS) and NiCo oxide (NCO-YS), respectively. Additionally, the elemental mapping images, as shown in Fig. S5, further validate these compositions by demonstrating the uniform distribution of each element.

XPS analysis was used to examine the chemical valence and surface compositions of NCSe-YS, NCSe@NCSeO-YS, NCSeO@NCO-YS, and NCO-YS, with the results presented in Fig. 3 and Fig. S6. In Fig. 3a, distinct Ni $2p_{3/2}$ and Ni $2p_{1/2}$ doublets for both nickel selenide and nickel selenite and their satellite peaks (marked as "Sat.") can be observed. The Ni 2*p* spectrum exhibited Ni $2p_{3/2}$ and Ni $2p_{1/2}$ at binding energies of 852.8 and 870.1 eV, respectively, corresponding to the typical Ni-Se bonding [30,31]. Additionally, the strong reactivity of nickel selenide with oxygen led to partial oxidation, forming nickel selenite. This is evidenced by the peaks observed at 855.0 and 873.2 eV [32]. The Co 2p spectrum revealed two prominent peaks corresponding to cobalt selenide at 778.1 and 793.1 eV, and two peaks for partially oxidized cobalt selenite at 780.2 and 796.2 eV [33–35]. Fig. 3c presents the Se 3d spectrum, which features a prominent peak that can be deconvoluted into two distinct peaks at 54.3 and 55.3 eV. These peaks are attributed to Se $3d_{5/2}$ and Se $3d_{3/2}$ and suggest the presence of NiCo selenide phase. [35,36]. The peaks observed at 58.7 and 60.2 eV are related to NiCo selenite phase due to the partial oxidation [37]. After oxidation at 400, 450, and 500 °C, yolk-shell microspheres exhibited clearly different Ni 2p, Co 2p, and Se 3d spectra comparing to those of NCSe-YS. In the Ni 2p spectra, Ni $2p_{3/2}$ and Ni $2p_{1/2}$ peaks associated with nickel selenite and nickel oxide gradually appeared as the oxidation temperature increased. The fitted peaks of Ni $2p_{3/2}$ and Ni $2p_{1/2}$ at binding energies of 853.7, 871.1 eV, and 855.3, 872.8 eV were corresponded to nickel selenide and nickel selenite, respectively as shown in Fig. 3d. From 450 °C oxidation, nickel oxide-related peaks were observed at binding energies of 855.5 and 857.5 eV (Ni $2p_{3/2}$) and 873.0 and 875.0 eV (Ni $2p_{1/2}$) as shown in Fig. S6a and S6d [38,39]. The fitted peaks of Co $2p_{3/2}$ and Co $2p_{1/2}$ exhibited similar appearance. The binding energies of 778.1, 794.0 eV, and 780.4, 796.5 eV were corresponded to cobalt selenide and cobalt selenite, respectively, from 450 °C oxidation, cobalt oxide-related peaks were observed at binding energies of 780.4, 782.4 eV (Co $2p_{3/2}$) and 796.5 and 798.2 (Co $2p_{1/2}$) as shown in Fig. S6b and S6e [40,41]. As compared to Se 3d peak of NCSe-YS in Fig. 3c, the peaks of metal selenite clearly represented after oxidation process as shown in Fig. 3f. The O 1 s spectra, shown in Fig. S6c and S6f, were analyzed to reveal three distinct peaks at 530.2, 531.4, and 533.1 eV. These peaks correspond to lattice oxygen (O1), adsorbed oxygen at surface vacancies (O2), and oxygen in physisorbed or chemisorbed water (O3), respectively [42]. For samples oxidized at 450 °C, a peak related to metal selenite was identified in O 1 s (Fig. S6c), which is supported by the XRD result in Fig. 2e. To demonstrate the thermal

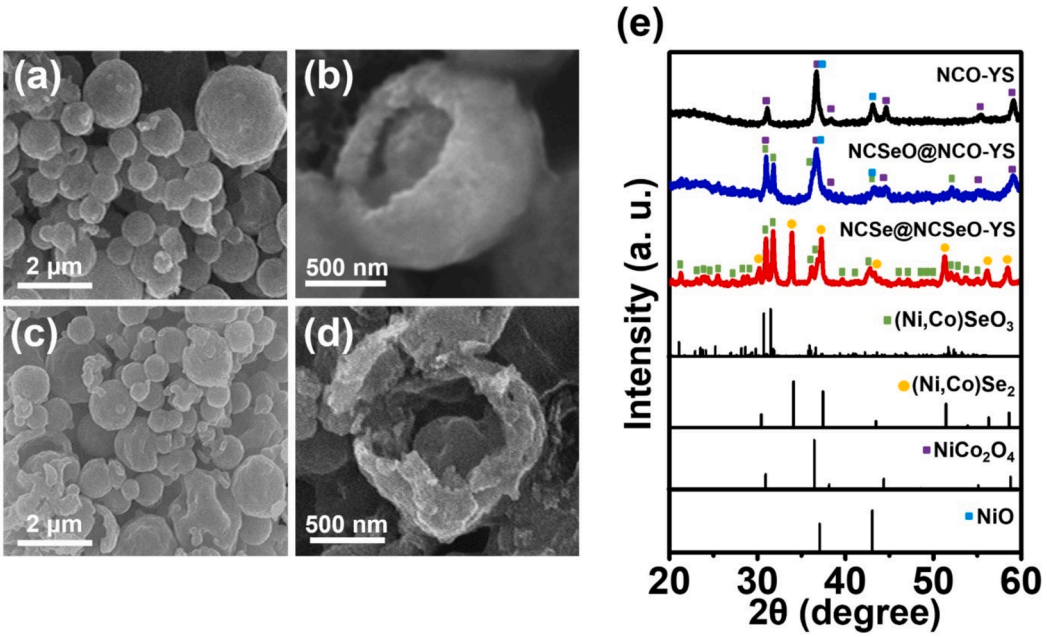

Fig. 2. SEM images of (a,b) NCSeO@NCO-YS and (c,d) NCO-YS samples. (e) XRD patterns of NCSe@NCSeO-YS, NCSeO@NCO-YS, and NCO-YS samples.

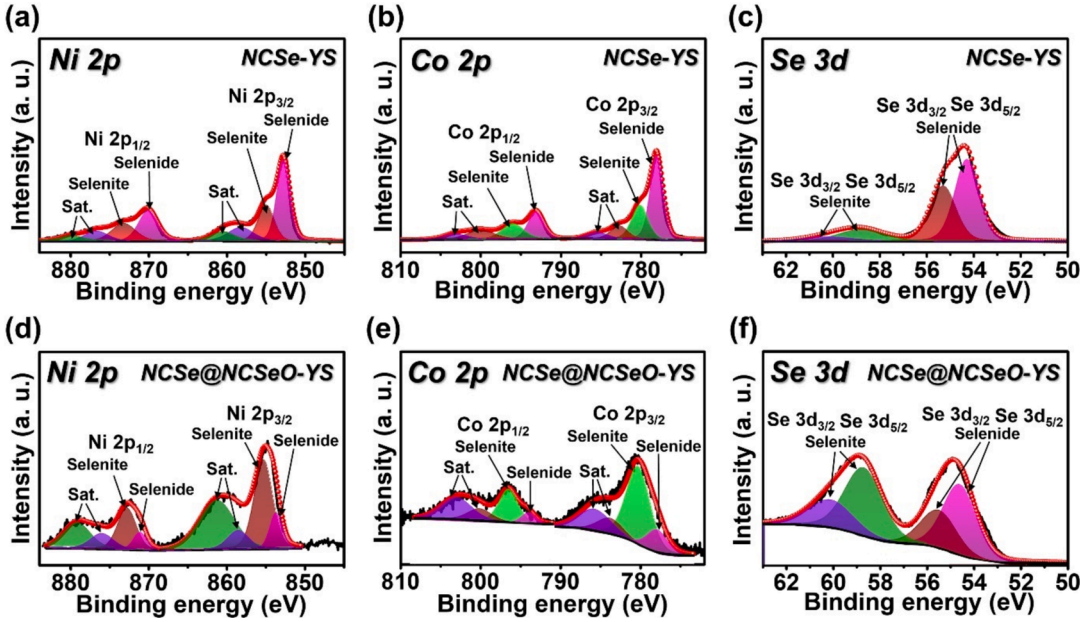

Fig. 3. XPS spectra of (a-c) NCSe-YS and (d-f) NCSe@NCSeO-YS samples corresponding to (a,d) Ni 2p, (b,e) Co 2p, and (c,f) Se 3d.

stability of developed material, thermogravimetric (TG) analysis on NCSe@NCSeO-YS and NCSe-YS samples was conducted, as shown in Fig. S7. The TG curves of both samples exhibited weight loss patterns above approximately 400 °C, attributed to the conversion of metal selenide or selenite into metal oxide. Interestingly, compared to NCSe-YS, NCSe@NCSeO-YS exhibited a phase transition at relatively higher temperatures. This behavior is attributed to the presence of the selenite phase in NCSe@NCSeO-YS, indicating that the NiCo selenide@NiCo selenite core–shell structure not only enhances the electrochemical performance but also improves the thermal stability of the material.

In this study, the oxidation process at 400 °C demonstrated that metal selenide materials can be partially oxidized to form a metal selenite phase. Furthermore, when the oxidation process was conducted at higher temperatures, the metal selenite phase was completely oxidized to form a metal oxide phase. This suggests that excessively high temperatures during oxidation should be avoided to ensure the formation of the selenite phase. From this perspective, it is also essential to investigate the effect of atmosphere and heat treatment time on the phase transition behavior. First, the oxidation process previously conducted at 400 °C in an air atmosphere was modified by replacing the air atmosphere with an Ar atmosphere for post-treatment. As shown in Fig. S8, unlike in the air atmosphere, the metal selenide materials did not undergo oxidation under the Ar atmosphere, and some metallic phases (Ni or Co) were observed. This indicates that the presence of oxygen in an air atmosphere is essential for forming metal selenite. Additionally, the effect of oxidation time was evaluated by conducting oxidation at 400 °C for 3 h and 15 h, referred to as 400 °C 3 hr and 400 °C 15 hr, respectively. As shown in Fig. S9, the XRD pattern of the

400 °C 3 hr sample primarily exhibited peaks corresponding to the selenide phase, along with weak peaks indicative of the selenite phase. In contrast, the XRD result of the 400 °C 15 hr sample revealed distinct peaks corresponding to the selenite phase, while also showing the presence of some oxide phase. These findings demonstrate that, in addition to appropriate temperature and atmosphere, time is also a critical factor in forming the metal selenite/metal selenide interface. Furthermore, our synthesis conditions are shown to represent optimal synthesis conditions for achieving this interface.

Cylic voltammetry (CV) was conducted at a scan rate of 0.1 mV s^{-1} within the potential range of 0.001–3.0 V for five cycles, to assess the capacity for sodium ion storage in yolk-shell microspheres containing nickel cobalt selenide, selenite, and oxide, as illustrated in Fig. 4. The CV curve of NCSe@NCSeO-YS (Fig. 4a) showed several cathodic and anodic peaks corresponding to electrochemical reaction of NiCo selenide and NiCo selenite and sodium ions. The broad cathodic peak near 0.75 V observed during the initial discharge process is attributed to the reduction of NiCo selenide to metallic Ni, Co, and Na_2Se, in addition to the conversion of NiCo selenite into metallic Ni, Co, Se, and Na_2O [43,44]. Therewith, selenium is sodiated, resulting in the formation of Na_2Se. Simultaneously, reduction peaks at around 0.75 V were also corresponded to formation of solid electrolyte interphases (SEI) layer [44]. During the initial anodic scan, the first small oxidation peak at 1.3 V was linked to the oxidation of metallic Ni and Co to their respective oxides (nickel and cobalt) as well as the decomposition of Na_2O [43]. The final oxidation peak at 2.1 V was corresponded to conversion of metallic Ni and Co phases back into NiCo selenide as well as the oxidation of Na_2Se into Se and some Se into SeO_2 [45]. After the initial cycle, multiple heterointerfaced $NiSe_x/CoSe_x/NiO/CoO_x/SeO_2/Se$ yolk-shell microspheres electrode was formed, which facilitated to enhanced sodium ion storage properties. After the initial cycle, all the redox reaction peaks were relevant to reversible conversion reaction of $NiSe_x$, $CoSe_x$, NiO, CoO_x, SeO_2, and Se with sodium ion. The CV curves of NCSeO@NCO-YS and NCO-YS exhibited similar cathodic and anodic peaks during the discharging and charging processes. In the initial discharging process, the small cathodic peak at 1.0 V was commonly related to the formation of sodium intercalated compounds for NiCo oxide [46]. The cathodic peak at 1.0 V of NCSeO@NCO-YS was additionally attributed to reduction of NiCo selenite to NiCo oxide and Na_2Se. The obvious sharp cathodic peak at 0.1 V represented to reduction of NiCo oxide to metallic Co, Ni, and Na_2O [47]. In subsequent anodic scan, both electrodes exhibited two oxidation peaks at 0.8 and 1.3 V. These peaks correspond to the oxidation of metallic Ni and Co to their respective oxides and the decomposition of Na_2O. [48]. As for the NCSeO@NCO-YS, small oxidation peak at 1.9 V were observed, which were related to the oxidation of Na_2Se into Se and some Se into SeO_2. Typically, a significant drop in the current at the cathodic peak between the 1st and 2nd cycles suggests a loss of irreversible capacity. However, it is notable that between the second and fifth cycles, both the peak intensity and the area under the CV curves progressively rise, reflecting an enhancement in the electrochemical reversibility.

To further validate the electrochemical reaction mechanism, ex-situ XRD analysis was performed on NCSe@NCSeO-YS electrode in its fully discharged and charged states. Fig. S10 presents the XRD patterns of the fully discharged NCSe@NCSeO-YS (denoted as NCSe@NCSeO-YS-D) and the fully charged NCSe@NCSeO-YS (denoted as NCSe@NCSeO-YS-C). During the initial discharging process, the NCSe@NCSeO-YS anode underwent a transformation into the ultrafine Ni/Co nanocrystals dispersed within the Na_2Se/Na_2O matrix. As reported in previous studies, the discharged products formed through the conversion reactions of metal chalcogenides typically exhibit low crystallinity, leading to weak XRD peaks [49,50]. Nevertheless, the XRD pattern of the NCSe@NCSeO-YS-D electrode showed distinct peaks corresponding to metallic Ni and Co, allowing for their identification to some extent. Additionally, SEI layers primarily composed of NaOH and NaF were observed. After the subsequent charging process, the NCSe@NCSeO-YS-C electrode displayed peaks corresponding to various phases, including metal oxides, metal selenides, and selenium oxides. These results are well-aligned with the CV data, confirming the consistency of the observed electrochemical behavior.

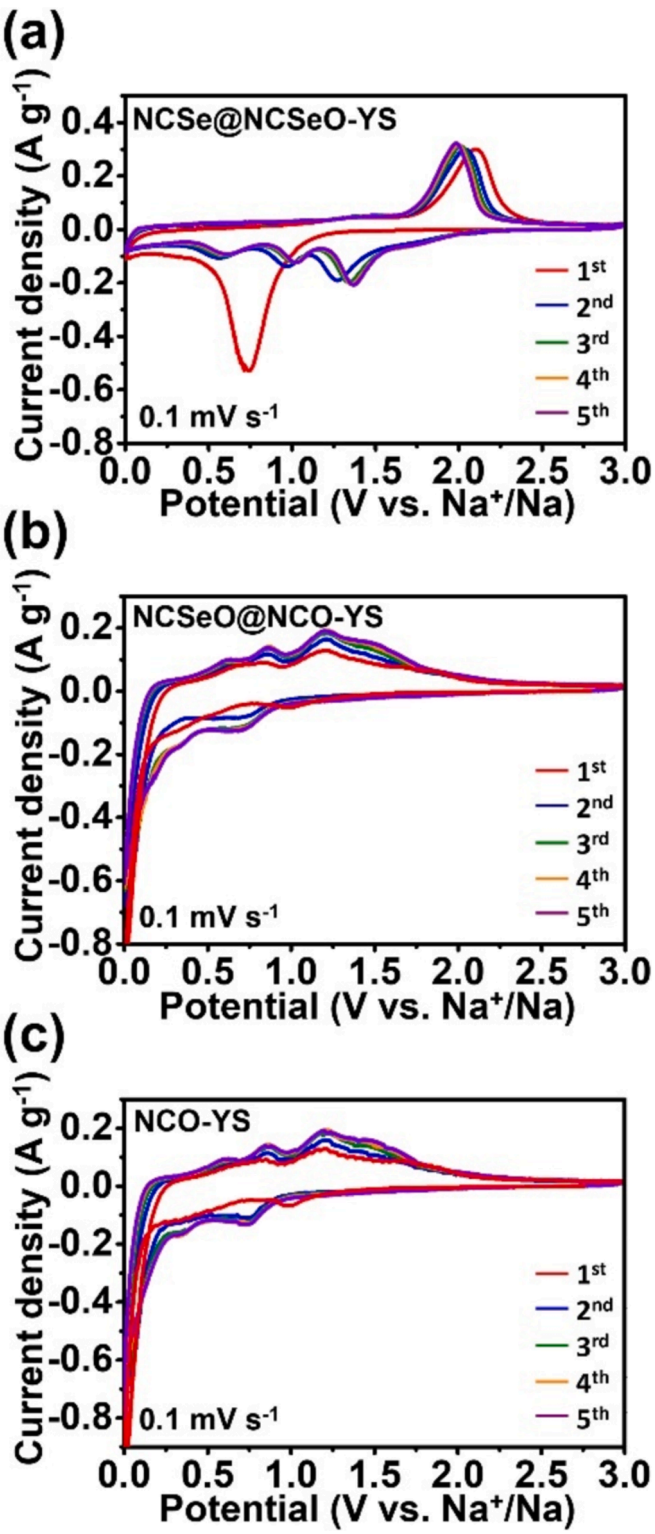

Fig. 4. CV curves of (a) NCSe@NCSeO-YS, (b) NCSeO@NCO-YS, and (c) NCO-YS electrodes.

In-situ EIS was employed to confirm the electrochemical reaction mechanisms of NCSe@NCSeO-YS, NCSeO@NCO-YS, and NCO-YS. Their electrochemical properties were compared at selected potentials during

the initial sodiation/desodiation stage, as illustrated in Fig. 5. Beginning at an open-circuit potential of 3.0 V, discharge and charge experiments were carried out within the voltage range of 0.001 to 3.0 V at a current density of 0.05 A g^{-1}. The colored dots in Fig. 5a-c represent the specific potentials selected for in-situ EIS measurements. The Nyquist plots show a depressed semicircle at high frequencies, another semicircle at mid frequencies, and a sloping line at low frequencies. The high- and mid-frequency semicircles correspond to interfacial resistance (R_{sei}, linked to the formation of SEI layers) and charge transfer resistance (R_{ct}), respectively, while the low-frequency sloped line is related to the diffusion of Na ions. The variation trends of total resistance (R_{tot}), which is the sum of R_s (solution resistance), R_{sei}, and R_{ct}, were observed as shown in Fig. 5d-f. Three oxidized yolk-shell microspheres electrodes exhibited similar variations of R_{tot} values during the initial discharging/charging stage. At the beginning, the R_{tot} value dropped sharply to 1.0 V, likely due to the aging of sodium ions that triggered the initial sodiation process, despite the ample aging period of 12 h [51]. At reduction to 1.0 V, the rapid decrease in R_{tot} value has been alleviated because of structural stress resulting from volume expansion via the conversion reaction of NiCo selenide and NiCo selenite with Na ions, which possessed resistance characteristics [52]. During the subsequent charging process, the R_{tot} was gradually sustained and showed a slight increase from 1.3 to 1.9 V. This change is attributed to the structural strain caused by the conversion reaction of NiCo selenide or NiCo oxide. However, the formation of multiple heterointerfaced $NiSe_x/CoSe_x/NiO/CoO_x/SeO_2/Se$ influenced low resistance value even though reformation of nickel cobalt compounds after the charging process [53]. The sodium diffusion coefficients for the three samples were assessed based on the in-situ EIS results presented in Fig. 5g-i. The Na-ion diffusion coefficient (D_{Na+}) can be calculated using the equation below:

$$D_{Na+} = 0.5\left(RT/Sn^2F^2C\sigma\right)^2$$

Comprehensive details on parameter values are available in earlier research [54]. The variation trends of the sodium diffusion coefficient for the three samples were the opposite of the resistance values, as shown in Fig. 5d-f. In addition, the oxidized three yolk-shell microspheres exhibited similar variation trends of D_{Na+} during the initial cycle. After 1.0 V for discharging process, the D_{Na+} values consistently increased until discharging end, which was due to the formation of ultrafine metallic Ni and Co over the amorphous Na_2Se and Na_2O matrix [21,55]. It contributed to enhance the diffusion rate of sodium ions. Throughout the following charging process, D_{Na+} maintained a steady trend up to 1.3 V. The reduction of D_{Na+} from 1.3 to 1.9 V was due to the structural transformation induced by the conversion reaction of NiCo selenide or NiCo oxide, which hinder the movement of sodium ions. After charging process end, the rapid decrease in D_{Na+} value has been owing to formation of multiple heterointerfaced structures. Among the three oxidized yolk-shell microsphere electrodes, NCSe@NCSeO-YS exhibited the lowest R_{tot} values and the highest D_{Na+} value during the overall initial cycle. It revealed that yolk shell oxidized at 400 °C, where the most heterointerfaces ($NiSe_x/CoSe_x/NiO/CoO_x/SeO_2/Se$) were formed, showed excellent resistance and sodium diffusion characteristics during the initial cycle.

Comparative analysis of the electrochemical behavior of the three oxidized yolk-shell microspheres as anodes for SIBs highlighted the superior sodium ion storage properties of NCSe@NCSeO-YS, as illustrated in Fig. 6. Fig. 6a-c presents the initial discharge and charge potential profiles of the three electrodes measured at a current density of 0.2 A g^{-1}. Several plateaus observed in the initial discharge and charge curves

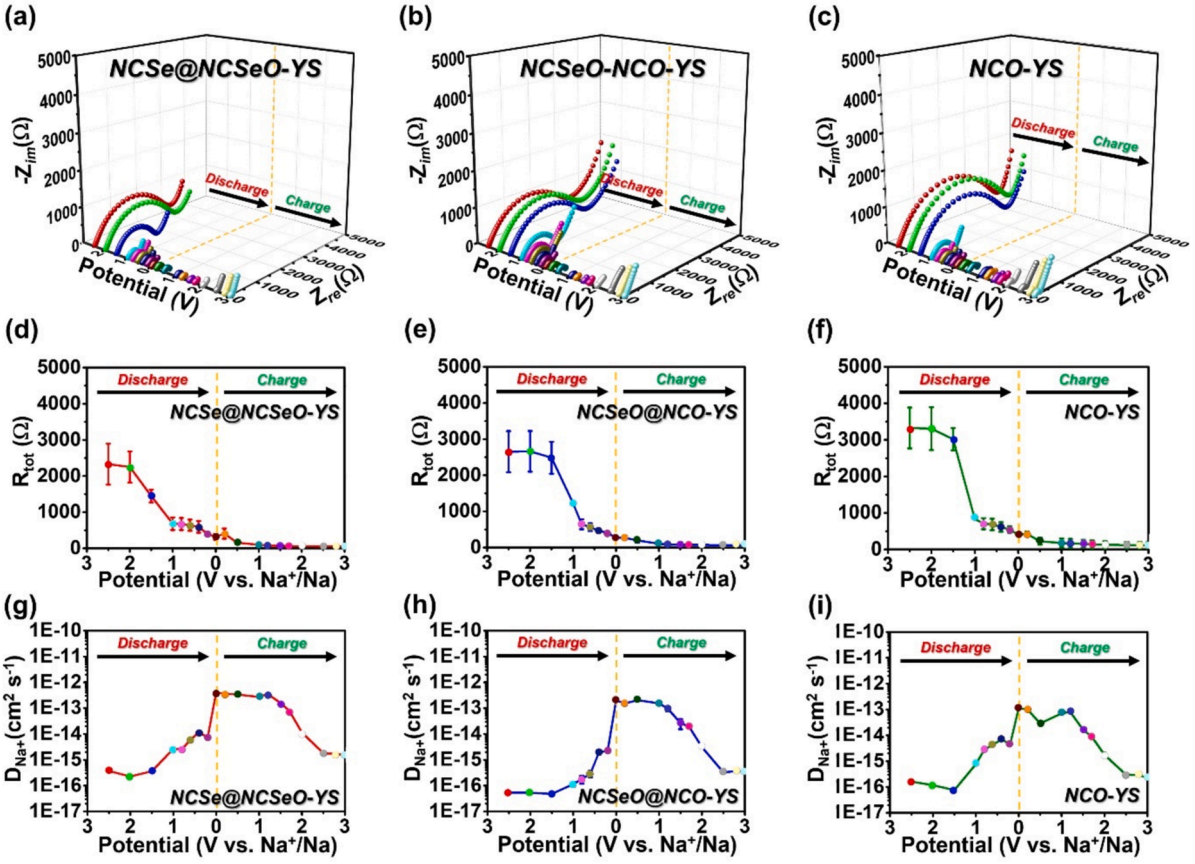

Fig. 5. (a-c) In-situ EIS Nyquist plots of NCSe@NCSeO-YS, NCSeO@NCO-YS, and NCO-YS measured at preselected potentials during the initial cycle, (d-f) in-situ EIS graphs (R_{tot} vs potential), and (g-i) variations in sodium-ion diffusion coefficients calculated from in-situ EIS results. The error bars originate from the standard deviation of calculated values. Each experiment was conducted three times to calculate the standard deviation values.

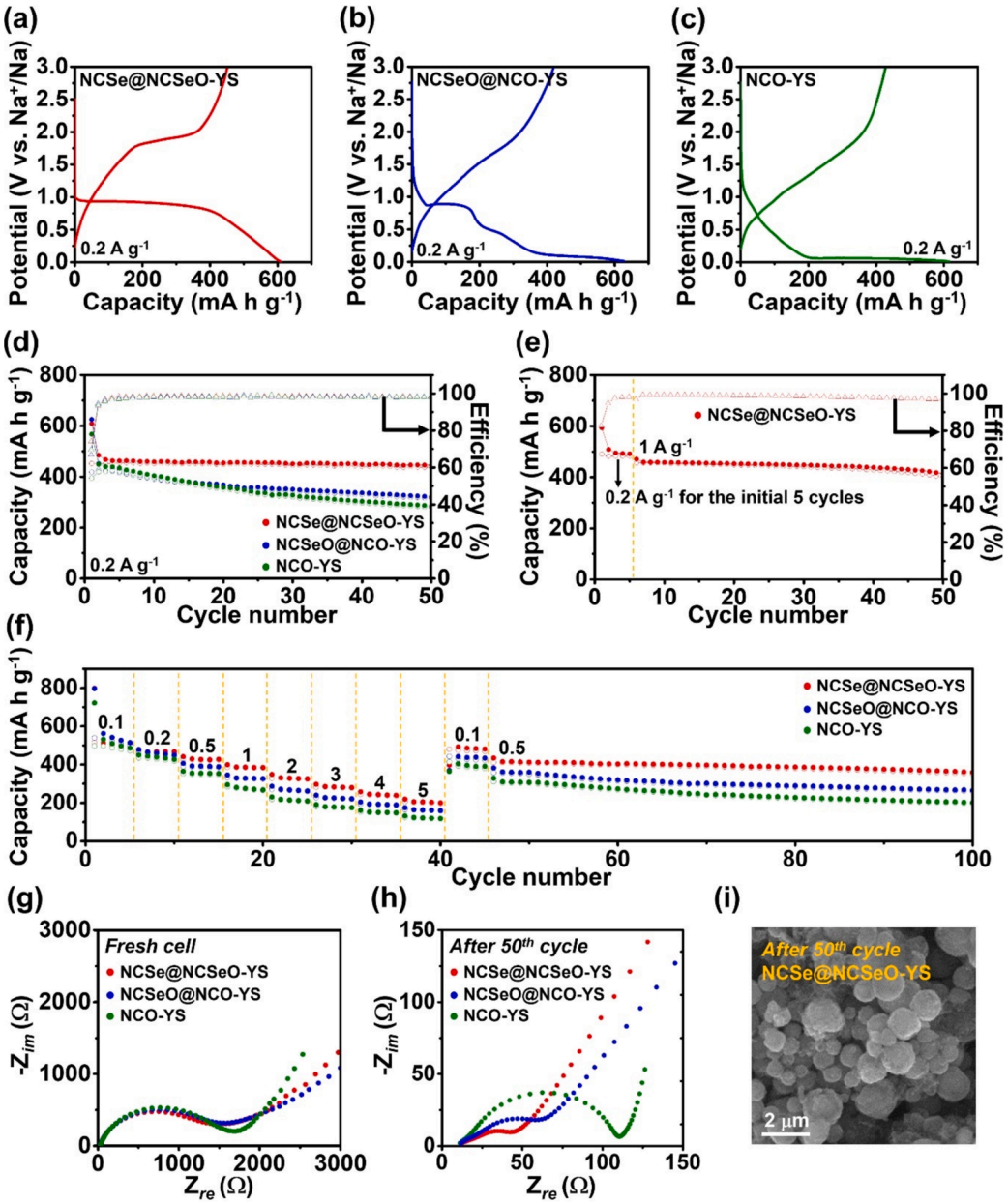

Fig. 6. Electrochemical properties of NCSe@NCSeO-YS, NCSeO@NCO-YS, and NCO-YS electrodes for SIBs. Initial discharge and charge curves of (a) NCSe@NCSeO-YS, (b) NCSeO@NCO-YS, and (c) NCO-YS, (d) cycle performances at a current density of 0.2 A g^{-1}, (e) cycle performance at a current density of 1 A g^{-1}, initially activated at a current density of 0.2 A g^{-1} for five cycles, (f) rate performances with subsequent cycling tests performed at a current density of 0.5 A g^{-1}. (g) Nyquist plots of fresh cells, (h) Nyquist plots after 100 cycles, (i) SEM image after 50 cycles of NCSe@NCSeO-YS.

of the three electrodes corresponded well with the CV results, as depicted in Fig. 4. The NCSe@NCSeO-YS, NCSeO@NCO-YS, and NCO-YS electrodes exhibited initial discharge capacities of 608, 627, and 615 mA h g^{-1}, respectively, with initial coulombic efficiencies (ICE) of 74, 67, and 70%, respectively. The cycling performances of NCSe-YS, NCSe@NCSeO-YS, NCSeO@NCO-YS, and NCO-YS at a current density of 0.2 A g^{-1} were shown in Fig. 6d and Fig. S11. NCSe-YS electrode exhibited a slight constant capacity decrease up to 50 cycles. The oxidized heterostructured NCSe@NCSeO-YS showed enhanced cyclic stability compared to NCSe-YS. It might be attributed to synergistic effect of formation of multiple heterointerfaced structures after cycling and construction of NiCo selenide@NiCo selenite hollow nanospheres *via* nanoscale Kirkendall diffusion which comprised yolk-shell microsphere. However, it was observed that the cycle stability deteriorated with increasing oxidation temperature. NCSeO@NCO-YS and NCO-YS electrodes, which were prepared at 450 and 500 °C, respectively, underwent more severe crystal growth as the oxidation temperature increases. Additionally, crystalized metal oxides react with sodium ions at a lower potential compared to metal selenides during the conversion reaction. This is because the metal-O bonds have higher binding energies than the metal–Se bonds. It indicated that metal oxide was kinetically disadvantageous in storage reaction with sodium ions compared to metal selenide, which contributed to cycle instability. After 50 cycles, the NCSe@NCSeO-YS electrode demonstrated a discharge capacity of 446 mA h g^{-1}, with a capacity retention of 92% starting from the second cycle. Additionally, the Coulombic efficiency approached nearly 99% by the 10th cycle and maintained high values through to the 50th cycle. In comparison, the discharge capacities NCSeO@NCO-YS and NCO-YS exhibited 322 and 286 mA h g^{-1}, respectively, while their capacity retentions from the second cycle were 71 and 64%,

respectively. Moreover, even at a high current density of 1 A g^{-1} (Fig. 6e), NCSe@NCSeO-YS showed excellent cycling stability, maintaining a discharge capacity of 414 mAh g^{-1} over 50 cycles. It demonstrated that the existence of multiple heterostructures improved the cycle stability since the volume change of active species at a certain potential was effectively alleviated by the mutual crystal growth relieving action. To assess the rate performance of oxidized yolk-shell microsphere electrodes, discharge and charge tests were conducted at varying rates from 0.1 to 5.0 A g^{-1}, as illustrated in Fig. 6f. NCSe@NCSeO-YS electrodes exhibited superior rate performance compared to the NCSeO@NCSe-YS and NCO-YS electrodes due to their distinctive multi-heterostructure and hollow nanosphere formation. This unique structure improved the surface reaction rates, optimized charge movement, and enabled rapid sodium-ion transport kinetics. NCSe@NCSeO-YS electrode showed reversible discharge capacities of 505, 468, 428, 385, 326, 280, 239, and 200 mA h g^{-1} at current densities of 0.1, 0.2, 0.5, 1, 2, 3, 4, and 5 A g^{-1}, respectively. Additionally, the subsequent cycle stability test conducted at a current density of 0.5 A g^{-1} confirmed the excellent structural stability of NCSe@NCSeO-YS over 100 cycles. The excellent Na-ion storage properties of NCSe@NCSeO-YS were confirmed via ex-situ EIS measurements. In the fresh-cell state, NCSe@NCSeO-YS showed the lowest resistance value owing to the presence of relatively conductive NiCo selenide component as depicted in Fig. 6g. Even after 50 cycles, NCSe@NCSeO-YS retained its low R_{tot}

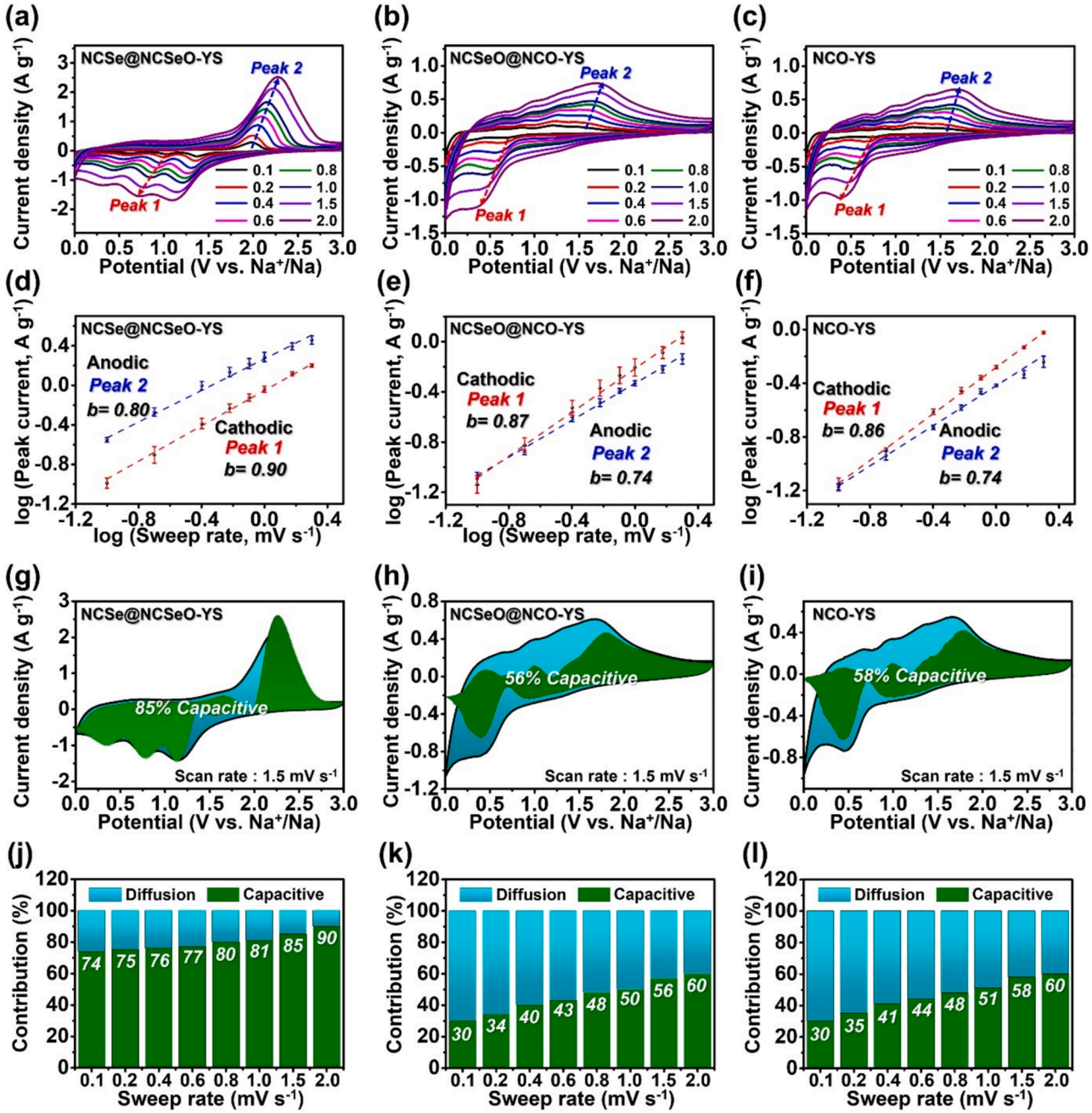

Fig. 7. CV curves of (a) NCSe@NCSeO-YS, (b) NCSeO@NCO-YS, and (c) NCO-YS at various scan rates, fitted log (peak current) vs. log (scan rate) for peak 1 and peak 2 for (d) NCSe@NCSeO-YS, (e) NCSeO@NCO-YS, and (f) NCO-YS, CV curves showing capacitive contribution (olive colored area) to the total current for (g) NCSe@NCSeO-YS, (h) NCSeO@NCO-YS, and (i) NCO-YS, and capacity contribution at different scan rates for (j) NCSe@NCSeO-YS, (k) NCSeO@NCO-YS, and (l) NCO-YS. The error bars originate from the standard deviation of calculated values. Each experiment was conducted three times to calculate the standard deviation values.

values, as shown in Fig. 6h. The R_{tot} values of, NCSe@NCSeO-YS, NCSeO@NCO-YS, and NCO-YS electrodes measured after the 50th cycle were 48, 72, and 112 Ω, respectively. The NCSe@NCSeO-YS demonstrated structural stability through repeated cycles of sodium insertion and extraction, which resulted from their minimal charge transfer resistance. To assess their durability, SEM images of the NCSe@NCSeO-YS after 50 cycles were examined, and the findings are presented in Fig. 6i. In contrast, the SEM images of NCSeO@NCO-YS and NCO-YS after 50 cycles revealed severe structural breaking, as depicted in Fig. S12.

To showcase the enhanced electrochemical kinetics of NCSe@NCSeO-YS, a series of CV tests were conducted on the three electrodes, as depicted in Fig. 7. With increasing scan rates, the CV curve peaks (Fig. 7a-c) became broader and experienced minor shifts, yet maintained their general form. These peak shifts are attributed to electrode polarization. The power-law relationship ($i_p = av^b$) between the peak current (i_p) and the scan rate (v) helps identify the charge storage mechanism, where a value of b = 1 indicates a capacitive process, and b = 0.5 signifies a diffusion-controlled process [56]. As shown in Fig. 7d-f, NiCo selenide@NiCo selenite yolk-shell microspheres exhibited higher b values during both the reduction (peak 1) and oxidation (peak 2) processes. Additionally, the capacitive contributions at different scan rates were determined using the following equation:

$$i(V) = k_1 v + k_2 v^{1/2}$$

The parameters $k_1 v$ and $k_2 v^{1/2}$ represent the surface capacitive and diffusion-controlled behaviors, respectively [57]. At a scan rate of 1.5 mV s^{-1} (Fig. 7g-i), the NiCo selenide@NiCo selenite yolk-shell microspheres displayed a capacitive contribution of 85%, which aligns with the observed high b values. In contrast, the other two electrodes showed comparatively lower capacitive contributions. Fig. 7j-l demonstrate that the NiCo selenide@NiCo selenite yolk-shell microspheres exhibited higher capacitive contributions across various scan rates, showing a consistent increase in capacitive contribution with increasing scan rates. This pronounced capacitive behavior underscores the synergistic effect between the heterointerface and the yolk-shell structure, consisting of hollow nanospheres, which promotes rapid Na ion transport and significantly enhances the rate capability.

4. Conclusions

In this study, we proposed newly designed multicomponent metal compounds with heterointerface structures and suggested their potential application as anode materials for sodium-ion batteries. By employing spray pyrolysis and post-treatment processes, yolk-shell structured microspheres consisting of heterogeneous NiCo selenide@-NiCo selenite core–shell nanospheres were successfully synthesized. This unique configuration effectively mitigates structural stress during the conversion reaction and enhances surface reaction kinetics. Furthermore, the heterointerface structure, induced by the conversion reaction of NiCo selenide@NiCo selenite nanocrystals, also improves sodium ion storage properties. Consequently, the combined advantages of the heterointerface and the yolk-shell architecture of the hollow nanospheres endows the material with robust cycling stability and excellent rate capabilities for sodium-ion batteries.

CRediT authorship contribution statement

Yeong Beom Kim: Writing – original draft, Investigation, Formal analysis, Data curation. **Seong-Yong Jeong:** Writing – original draft, Investigation, Formal analysis, Conceptualization. **Jung Sang Cho:** Formal analysis, Conceptualization. **Dong-Hee Lim:** Writing – review & editing, Investigation, Formal analysis, Data curation. **Yun Chan Kang:** Writing – review & editing, Supervision, Investigation. **Gi Dae Park:** Writing – review & editing, Writing – original draft, Supervision, Investigation, Conceptualization.

Declaration of competing interest

The authors declare that they have no known competing financial interests or personal relationships that could have appeared to influence the work reported in this paper.

Acknowledgments

This work was supported by the National Research Foundation of Korea (NRF) grant funded by the Korean government (MEST) (No. NRF-2022R1F1A1070886). This work was supported by the National Research Foundation of Korea (NRF) funded by the Korean government (MEST) (No. RS-2023-00217581). This work was supported by the Commercialization Promotion Agency for R&D Outcomes (COMPA) funded by the Ministry of Science and ICT of South Korea (Grant No. RS-2023-00304768). This work was supported by the Chungbuk National University BK21 program (2023). This work was supported by the research grant of Kongju National University in 2024.

Appendix A. Supplementary data

Supplementary data to this article can be found online at https://doi.org/10.1016/j.apsusc.2024.162094.

Data availability

No data was used for the research described in the article.

References

[1] X. Zhang, R. Bi, J. Wang, M. Zheng, J. Wang, R. Yu, D. Wang, Delicate co-control of shell structure and sulfur vacancies in interlayer-expanded tungsten disulfide hollow sphere for fast and stable sodium storage, Adv. Mater. 35 (2023) 2209354.
[2] C. Wu, H. Song, C. Tang, A. Du, C. Yu, Z. Huang, M. Wu, H. Zhang, Ultralarge interlayer distance and C, N-codoping enable superior sodium storage capabilities of MoS_2 nanoonions, Chem. Eng. J. 378 (2019) 122249.
[3] H. Li, M. Xu, Z. Zhang, Y. Lai, J. Ma, Engineering of polyanion type cathode materials for sodium-ion batteries: toward higher energy/power density, Adv. Funct. Mater. 30 (2020) 2000473.
[4] J.-Y. Hwang, S.-T. Myung, Y.-K. Sun, Sodium-ion batteries: present and future, Chem. Soc. Rev. 46 (2017) 3529–3614.
[5] M. Liu, J. Xu, L. Shao, X. Shi, C. Li, Z. Sun, Towards metal selenides: A promising anode for sodium-ion batteries, Chem. Commun. (2024).
[6] Y. Gong, Y. Li, Y. Li, M. Liu, X. Feng, Y. Sun, F. Wu, C. Wu, Y. Bai, Unraveling the intrinsic origin of the superior sodium-ion storage performance of metal selenides anode in ether-based electrolytes, Nano Lett. (2024).
[7] Y. Gong, Y. Li, Y. Li, M. Liu, Y. Bai, C. Wu, Metal selenides anode materials for sodium ion batteries: synthesis, modification, and application, Small 19 (2023) 2206194.
[8] D. Yu, X. Wei, D. Zhao, S. Gao, G. Zhao, H. Zhang, Z. Li, M. Yu, Y. Sun, Ultrathin CuSe nanosheets as the anode for sodium ion battery with high rate performance and long cycle life, Electrochim. Acta 404 (2022) 139703.
[9] N. Buğday, H. Wang, N. Hong, B. Zhang, W. Deng, G. Zou, H. Hou, S. Yaşar, X. Ji, Fabrication of a stable and highly effective anode material for Li-ion/Na-ion batteries utilizing ZIF-12, Small (2024).
[10] H. Kim, T.-H. Kim, G.-B. Cho, H.-S. Ryu, J.-H. Ahn, K.-K. Cho, H.-J. Ahn, Facile synthesis of binder-free CuSe as a long-cycling anode for sodium batteries: Self-healing metal selenide anode for sodium batteries, J. Energy Storage 76 (2024) 109848.
[11] H. Zhou, X. Li, Y. Li, M. Zheng, H. Pang, Applications of MxSey (M= Fe Co, Ni) and their composites in electrochemical energy storage and conversion, Nano-Micro Lett. 11 (2019) 1–33.
[12] Q. Pan, M. Zhang, L. Zhang, Y. Li, Y. Li, C. Tan, F. Zheng, Y. Huang, H. Wang, Q. Li, $FeSe_2$@C microrods as a superior long-life and high-rate anode for sodium ion batteries, ACS Nano 14 (2020) 17683–17692.
[13] Z. Hao, X. Shi, Z. Yang, L. Li, S.L. Chou, Developing high-performance metal selenides for sodium-ion batteries, Adv. Funct. Mater. 32 (2022) 2208093.
[14] H. Wu, R. Yuan, M. Li, L. Liu, Y. Liu, Q. Song, W. Ai, H. Du, Z. Du, K. Wang, $Co_{0.85}Se$–fe_7Se_8 Nanocuboids Embedded in Reduced Graphene Oxides as Cycle-Stable Anodes for Sodium-Ion Batteries 198 (2022) 171–178.
[15] P. Liu, J. Han, K. Zhu, Z. Dong, L. Jiao, Heterostructure $SnSe_2$/ZnSe@PDA nanobox for stable and highly efficient sodium-ion storage, Adv. Energy Mater. 10 (2020) 2000741.

[16] B. Cong, X. Li, Y. Suo, G. Chen, Metal–organic framework derived bimetallic selenide embedded in nitrogen-doped carbon hierarchical nanosphere for highly reversible sodium-ion storage, J. Colloid Interface Sci. 635 (2023) 370–378.
[17] J.E. Zhou, R.C.K. Reddy, A. Zhong, Y. Li, Q. Huang, X. Lin, J. Qian, C. Yang, I. Manke, R. Chen, Metal–organic framework-based materials for advanced sodium storage: Development and anticipation, Adv. Mater. 36 (2024) 2312471.
[18] P. Zhou, L. Wang, M. Zhang, Q. Huang, Z. Su, X. Wang, D. Guo, M. Liao, P. Xu, X. Lin, Hierarchical structural modulation and Co-Construction of selenium vacancy in ZnSe/$NiSe_2$ heterojunctions to enhance cycling stability and fast ion diffusion kinetics for lithium-ion and sodium-ion batteries, Chem. Eng. J. 488 (2024) 150829.
[19] M. Wang, A. Peng, J. Jiang, M. Zeng, Z. Yang, J. Chen, B. Guo, Z. Ma, B. Yu, Y. Zhang, Heterointerface synergistic Na^+ storage fundamental mechanism for $CoSeO_3$ playing as anode for sodium ion batteries/capacitors, Chem. Eng. J. 433 (2022) 134567.
[20] C.C. Weng, J.T. Ren, Z.Y. Yuan, Transition metal phosphide-based materials for efficient electrochemical hydrogen evolution: a critical review, ChemSusChem 13 (2020) 3357–3375.
[21] J.-T. Ren, G.-G. Yuan, C.-C. Weng, L. Chen, Z.-Y. Yuan, Uniquely integrated Fe-doped $Ni(OH)_2$ nanosheets for highly efficient oxygen and hydrogen evolution reactions, Nanoscale 10 (2018) 10620–10628.
[22] J.-T. Ren, L. Chen, D.-D. Yang, Z.-Y. Yuan, Molybdenum-based nanoparticles (Mo_2C, MoP and MoS_2) coupled heteroatoms-doped carbon nanosheets for efficient hydrogen evolution reaction, Appl. Catal. B 263 (2020) 118352.
[23] J.-T. Ren, Y.-S. Wang, L. Chen, L.-J. Gao, W.-W. Tian, Z.-Y. Yuan, Binary FeNi phosphides dispersed on N, P-doped carbon nanosheets for highly efficient overall water splitting and rechargeable Zn-air batteries, Chem. Eng. J. 389 (2020) 124408.
[24] J.-T. Ren, C.-Y. Wan, T.-Y. Pei, X.-W. Lv, Z.-Y. Yuan, Promotion of electrocatalytic nitrogen reduction reaction on N-doped porous carbon with secondary heteroatoms, Appl. Catal. B 266 (2020) 118633.
[25] J.-T. Ren, Z.-Y. Yuan, Hierarchical nickel sulfide nanosheets directly grown on Ni foam: a stable and efficient electrocatalyst for water reduction and oxidation in alkaline medium, ACS Sustain. Chem. Eng. 5 (2017) 7203–7210.
[26] K. Li, W. Chen, L. Ma, X. Zhang, J. Guo, L. Yang, Advanced sodium storage of carbon coated Co-$MoSe_2$ nanosheets assembled spheres, J. Energy Storage 84 (2024) 110933.
[27] X. Zhao, H.-E. Wang, Y. Yang, Z.G. Neale, R.C. Massé, J. Cao, W. Cai, J. Sui, G. Cao, Reversible and fast Na-ion storage in MoO_2/$MoSe_2$ heterostructures for high energy-high power Na-ion capacitors, Energy Storage Mater. 12 (2018) 241–251.
[28] Y.B. Kim, H.Y. Seo, T.G. Senthamaraikannan, J.S. Cho, Y.C. Kang, D.-H. Lim, G. D. Park, One-step synthesis of zinc oxide-carbon microspheres decorated with multi-voids and carbon nanotubes via spray pyrolysis for enhanced stability in lithium metal anodes, J. Mater. Sci. Technol. 192 (2024) 95–107.
[29] G.D. Park, J.S. Cho, Y.C. Kang, Novel cobalt oxide-nanobubble-decorated reduced graphene oxide sphere with superior electrochemical properties prepared by nanoscale Kirkendall diffusion process, Nano Energy 17 (2015) 17–26.
[30] R. Gao, G.-D. Li, J. Hu, Y. Wu, X. Lian, D. Wang, X. Zou, In situ electrochemical formation of NiSe/NiO_x core/shell nano-electrocatalysts for superior oxygen evolution activity, Catal, Sci. Technol. 6 (2016) 8268–8275.
[31] H. Mei, Z. Huang, B. Xu, Z. Xiao, Y. Mei, H. Zhang, S. Zhang, D. Li, W. Kang, D. F. Sun, $NiSe_2$/$Ni(OH)_2$ heterojunction composite through epitaxial-like strategy as high-rate battery-type electrode material, Nano-Micro Lett. 12 (2020) 1–15.
[32] G.D. Park, J.H. Hong, S.-K. Park, Y.C. Kang, Strategy for synthesizing mesoporous NiO polyhedra with empty nanovoids via oxidation of NiSe polyhedra by nanoscale Kirkendall diffusion and their superior lithium-ion storage performance, Appl. Surf. Sci. 464 (2019) 597–605.
[33] H. Zhang, T. Wang, A. Sumboja, W. Zang, J. Xie, D. Gao, S.J. Pennycook, Z. Liu, C. Guan, J. Wang, Integrated hierarchical carbon flake arrays with hollow P-doped $CoSe_2$ nanoclusters as an advanced bifunctional catalyst for Zn–air batteries, Adv. Funct. Mater. 28 (2018) 1804846.
[34] H. Li, D. Gao, X. Cheng, Simple microwave preparation of high activity Se-rich $CoSe_2$/C for oxygen reduction reaction, Electrochim. Acta 138 (2014) 232–239.
[35] S.H. Yang, S.-K. Park, Y.C. Kang, MOF-derived $CoSe_2$@N-doped carbon matrix confined in hollow mesoporous carbon nanospheres as high-performance anodes for potassium-ion batteries, Nano-Micro Lett. 13 (2021) 1–15.
[36] P.E. Karthik, H. Rajan, V.R. Jothi, M.J. Ko, S.C. Yi, Enhanced electrochemical oxygen evolution reaction on hydrogen embrittled CoSe surface, Adv. Mater. Interfaces 9 (2022) 2101209.
[37] Q.-S. Jiang, W. Li, J. Wu, W. Cheng, J. Zhu, Z. Yan, X. Wang, Y. Ju, Electrodeposited cobalt and nickel selenides as high-performance electrocatalytic materials for dye-sensitized solar cells, J. Mater. Sci.: Mater. Electron. 30 (2019) 9429–9437.
[38] U. De Silva, J. See, W.P. Liyanage, J. Masud, J. Wu, W. Yang, W.-T. Chen, D. Prendergast, M. Nath, Understanding the structural evolution of a nickel chalcogenide electrocatalyst surface for water oxidation, Energy Fuels 35 (2021) 4387–4403.
[39] W. Zhang, H. Shen, M. Yin, L. Lu, B. Xu, D. Li, Heterostructure silicon solar cells with enhanced power conversion efficiency based on Si_x/Ni^{3+} self-doped NiO_x passivating contact, ACS Omega 7 (2022) 16494–16501.
[40] Y.B. Kim, H.Y. Seo, S.H. Kim, T.H. Kim, J.H. Choi, J.S. Cho, Y.C. Kang, G.D. Park, Controllable synthesis of carbon yolk-shell microsphere and application of metal compound–carbon yolk-shell as effective anode material for alkali-ion batteries, Small Methods 7 (2023) 2201370.
[41] J.X. Flores-Lasluisa, J. Quílez-Bermejo, A.C. Ramírez-Pérez, F. Huerta, D. Cazorla-Amorós, E. Morallón, Copper-doped cobalt spinel electrocatalysts supported on activated carbon for hydrogen evolution reaction, Mater. 12 (2019) 1302.
[42] A.B. Urgunde, V. Kamboj, H.P. Kannattil, R. Gupta, Layer-by-layer coating of cobalt-based ink for large-scale fabrication of OER electrocatalyst, Energy Technol. 7 (2019) 1900603.
[43] J.-S. Park, G.D. Park, Y.C. Kang, Exploration of cobalt selenite–carbon composite porous nanofibers as anode for sodium-ion batteries and unveiling their conversion reaction mechanism, J. Mater. Sci. Technol. 89 (2021) 24–35.
[44] L.-C. Qiu, Q.-C. Wang, X.-Y. Yue, Q.-Q. Qiu, X.-L. Li, D. Chen, X.-J. Wu, Y.-N. Zhou, $NiCo_2Se_4$ as an anode material for sodium-ion batteries, Electrochem. Commun. 112 (2020) 106684.
[45] G.D. Park, S.J. Yang, J.H. Lee, Y.C. Kang, Investigation of binary metal (Ni, Co) selenite as Li-ion battery anode materials and their conversion reaction mechanism with Li ions, Small 15 (2019) 1905289.
[46] Y. Zhang, N. Wang, Z. Bai, The progress of cobalt-based anode materials for lithium ion batteries and sodium ion batteries, Appl. Sci. 10 (2020) 3098.
[47] P.-P. Chen, H.-B. Guan, B.-H. Zhang, J.-T. Lei, Z.-A. Li, Y.-L. Hou, J.-Z. Chen, D.-L. Zhao, Graphene encapsulated NiO-Co_3O_4 open-ended hollow nanocube anode with enhanced performance for lithium/sodium ion batteries, J. Alloys Compd. 979 (2024) 173479.
[48] M. Chen, X. Xia, J. Yin, Q. Chen, Construction of Co_3O_4 nanotubes as high-performance anode material for lithium ion batteries, Electrochim. Acta 160 (2015) 15–21.
[49] Q. Su, J. Zhang, Y. Wu, G. Du, Revealing the electrochemical conversion mechanism of porous Co_3O_4 nanoplates in lithium ion battery by in situ transmission electron microscopy, Nano Energy 9 (2014) 264–272.
[50] L. Luo, J. Wu, J. Xu, V.P. Dravid, Atomic resolution study of reversible conversion reaction in metal oxide electrodes for lithium-ion battery, ACS Nano 8 (2014) 11560–11566.
[51] Y.B. Kim, H.Y. Seo, K.H. Kim, J.S. Cho, Y.C. Kang, G.D. Park, Synthesis of iron sulfide nanocrystals encapsulated in highly porous carbon-coated CNT microsphere as anode materials for sodium-ion batteries, Small 20 (2024) 2305686.
[52] G.D. Park, J.-S. Park, J.K. Kim, Y.C. Kang, Metal sulfoselenide solid solution embedded in porous hollow carbon nanospheres as effective anode material for potassium-ion batteries with long cycle life and enhanced rate performance, Chem. Eng. J. 428 (2022) 131051.
[53] G.D. Park, Y. Chan Kang, Amorphous cobalt selenite nanoparticles decorated on a graphitic carbon hollow shell for high-rate and ultralong cycle life lithium-ion batteries, ACS Sustainable, Chem. Eng. 8 (2020) 17707–17717.
[54] Z. Wang, K. Dong, D. Wang, S. Luo, X. Liu, Y. Liu, Q. Wang, Y. Zhang, A. Hao, C. He, Constructing N-doped porous carbon confined FeSb alloy nanocomposite with Fe-NC coordination as a universal anode for advanced Na/K-ion batteries, Chem. Eng. J. 384 (2020) 123327.
[55] J. Zhang, J. Lin, Y. Zeng, Y. Zhang, H. Guo, Morphological and structural evolution of MnO@C anode and its application in lithium-ion capacitors, ACS Appl. Energy Mater. 2 (2019) 8345–8358.
[56] S. Iqbal, L. Wang, Z. Kong, Y. Zhai, X. Sun, F. Wang, Z. Jing, X. He, J. Dou, L. Xu, In situ growth of CoS_2/ZnS nanoparticles on graphene sheets as an ultralong cycling stability anode for potassium ion storage, ACS Appl. Mater. Interfaces 14 (2022) 15324–15336.
[57] P. Ge, H. Hou, S. Li, L. Huang, X. Ji, Three-dimensional hierarchical framework assembled by cobblestone-like $CoSe_2$@C nanospheres for ultrastable sodium-ion storage, ACS Appl. Mater. Interfaces 10 (2018) 14716–14726.